RESEARCH

Spectral CT-based radiomics signature for distinguishing malignant pulmonary nodules from benign

Hang Xu[1†], Na Zhu[2†], Yong Yue[1], Yan Guo[3], Qingyun Wen[4], Lu Gao[5], Yang Hou[1] and Jin Shang[1*]

Abstract

Objectives To evaluate the discriminatory capability of spectral CT-based radiomics to distinguish benign from malignant solitary pulmonary solid nodules (SPSNs).

Materials and methods A retrospective study was performed including 242 patients with SPSNs who underwent contrast-enhanced dual-layer Spectral Detector CT (SDCT) examination within one month before surgery in our hospital, which were randomly divided into training and testing datasets with a ratio of 7:3. Regions of interest (ROIs) based on 40-65 keV images of arterial phase (AP), venous phases (VP), and 120kVp of SDCT were delineated, and radiomics features were extracted. Then the optimal radiomics-based score in identifying SPSNs was calculated and selected for building radiomics-based model. The conventional model was developed based on significant clinical characteristics and spectral quantitative parameters, subsequently, the integrated model combining radiomics-based model and conventional model was established. The performance of three models was evaluated with discrimination, calibration, and clinical application.

Results The 65 keV radiomics-based scores of AP and VP had the optimal performance in distinguishing benign from malignant SPSNs ($AUC_{65keV-AP} = 0.92$, $AUC_{65keV-VP} = 0.88$). The diagnostic efficiency of radiomics-based model ($AUC = 0.96$) based on 65 keV images of AP and VP outperformed conventional model ($AUC = 0.86$) in the identification of SPSNs, and that of integrated model ($AUC = 0.97$) was slightly further improved. Evaluation of three models showed the potential for generalizability.

Conclusions Among the 40-65 keV radiomics-based scores based on SDCT, 65 keV radiomics-based score had the optimal performance in distinguishing benign from malignant SPSNs. The integrated model combining radiomics-based model based on 65 keV images of AP and VP with Z_{eff-AP} was significantly superior to conventional model in the discrimination of SPSNs.

Keywords Solitary pulmonary solid nodules, Discrimination, Dual-layer spectral detector CT, Radiomics

†Hang Xu and Na Zhu contributed equally to this work.

*Correspondence:
Jin Shang
895495103@qq.com
[1] Department of Radiology, Shengjing Hospital of China Medical University, Shenyang 110004, China
[2] Department of Radiation Oncology, Nanfang Hospital of Southern Medical University, Guangzhou 510000, China
[3] GE Healthcare, Shenyang 110004, China
[4] Department of Radiology, Jining First People's Hospital, Jining 272000, China
[5] Department of Radiology, Liaoning Province Cancer Hospital, Shenyang 110801, China

Introduction

At present, radiomics research based on traditional CT has revealed the potential to differentiate benign and malignant pulmonary nodules [1–9]. So far, few radiomics-based studies have applied different Dual-energy-CT (DECT) images for characterizing tumors, where the rich and additional quantitative information on the energy-dependent attenuation changes in different tissues could potentially improve performance of predictive models [10–12]. As an emerging and exciting DECT, Dual-layer Spectral Detector CT (SDCT) is proved to be a promising technology in oncologic identification [13–16]. Firstly, it collects high and low energy information and acquires in-phase, temporally synchronized, and homologous photons in a conventional CT scanning, which improves the accuracy of data collection. Secondly, SDCT exploits anti-correlated noise suppression [17], leading to a constantly low noise level [18]. Thirdly, SDCT eliminates the requirement to pre-select patients or change clinical workflow [19], permitting evaluation of incidentally discovered findings. Recent studies have shown that spectral quantitative parameters could further improve the discriminative ability of pulmonary nodules [20–24], such as CT values of 40 keV monochromatic images ($CT_{40\,keV}$), the slope of the spectral Hounsfield Unit curve (λ_{HU}), iodine concentration (IC), normalized iodine concentration (NIC), and the differences in NIC between the proximal and the distal regions in pulmonary nodules (dNIC). IC reflects the difference of blood supply within the lesions [22, 25, 26], and λ_{HU} presents the attenuation characteristics of different tissues [27]. Although the role of both in identifying benign and malignant nodules has been widely mentioned, studies on the selection of the optimal sequence of virtual monochromatic images (VMI) remain rare. Hence, we aimed to select the optimal sequence of VMI based on the latest SDCT for the first time and develop a spectral CT radiomics-based signature to differentiate solitary pulmonary solid nodules (SPSNs).

Materials and methods

Patients

The study population was retrospectively enrolled SPSNs patients who underwent contrast-enhanced SDCT examination within one month before surgery from our hospital between January 2016 and December 2020. Ultimately, 242 patients (average age 59.90 ± 10.55 years) were included. We collected 6 clinical risk factors including age, sex, smoking, carcinoembryonic antigen (CEA), cytokeratin 19 fragment 21–1 (CYFRA21-1), and neuron-specific enolase (NSE). The final cohort was randomly divided into training ($n = 168$) and testing datasets ($n = 74$) with a ratio of 7:3. An overview workflow of this study was shown in Fig. 1.

Image acquisition

Contrast-enhanced chest scans were performed in both arterial phase (AP) and venous phase (VP) on dual-layer spectral detector CT (IQon Spectral CT, Philips Healthcare, Best, The Netherlands). The range of scan was from the thoracic inlet to the bottom of the thoracic cavity in order to cover all lung tissues. After a native chest scan, contrast agent (Iodixanol, 350 mg/mL, GE Healthcare, Ireland) was injected via the cubital vein with a power injector (Ulrich REF XD 2051), at a volume of 80 ml and flow rate of 2.5 mL/s. AP and VP scans were acquired at 25 and 60 s after the contrast agent injection. Spectral CT scan parameters were as follows: tube voltage $= 120$ kV; automatic tube current exposure control [Dose Right Index (DRI)] $= 22$; tube rotation time $= 0.5$ s; detector collimation $= 64 \times 0.625$ mm; a reconstructed slice thickness $= 0.9$ mm; slice increment $= 0.45$ mm; field of view $= 250 \times 250$ mm; image reconstruction matrix $= 512 \times 512$. All original images were reconstructed as Spectral Base Image (SBI) datasets with reconstructed slice thickness of 1 mm and increment of 1 mm, then were transmitted to a dedicated post-processing workstation of spectral CT (IntelliSpace Portal 6.5, Philips Healthcare, Best, The Netherlands) for image analysis.

Spectral quantitative parameter measurement

Quantitative parameters of spectral CT were measured on the best-displayed plane and the relative homogeneous area of lesions in 40-65 keV images of AP, VP, and conventional 120kVp in the dedicated post-processing workstation (IntelliSpace Portal 6.5, PhilipsHealthcare, Best, The Netherlands). The following quantitative measurements were performed twice, and the average value was calculated. Quantitative parameters were as follows: (I) IC of the lesion (IC_{lesion}) and IC in the same layer of aorta (IC_{aorta}), calculated $NIC = IC_{lesion}/IC_{aorta}$; (II) effective atomic number (Z_{eff}); (III) CT values of 40 keV (CT_{40keV}) and 80 keV monochromatic images (CT_{80keV}); (IV) $\lambda_{HU} = |CT_{40keV} - CT_{80keV}|/(80-40)$.

Images segmentation

The original CT images were imported into the image preprocessing module of Artificial Intelligence Kit (A.K., GE Healthcare, China), then which were preprocessed to ensure that the voxel points of the images were isotropic. The preprocessed images were uploaded to ITK-SNAP software (http://www.itksnap.org), and the two-dimensional region of interest (ROI) was manually delineated on the single representative section that had the largest
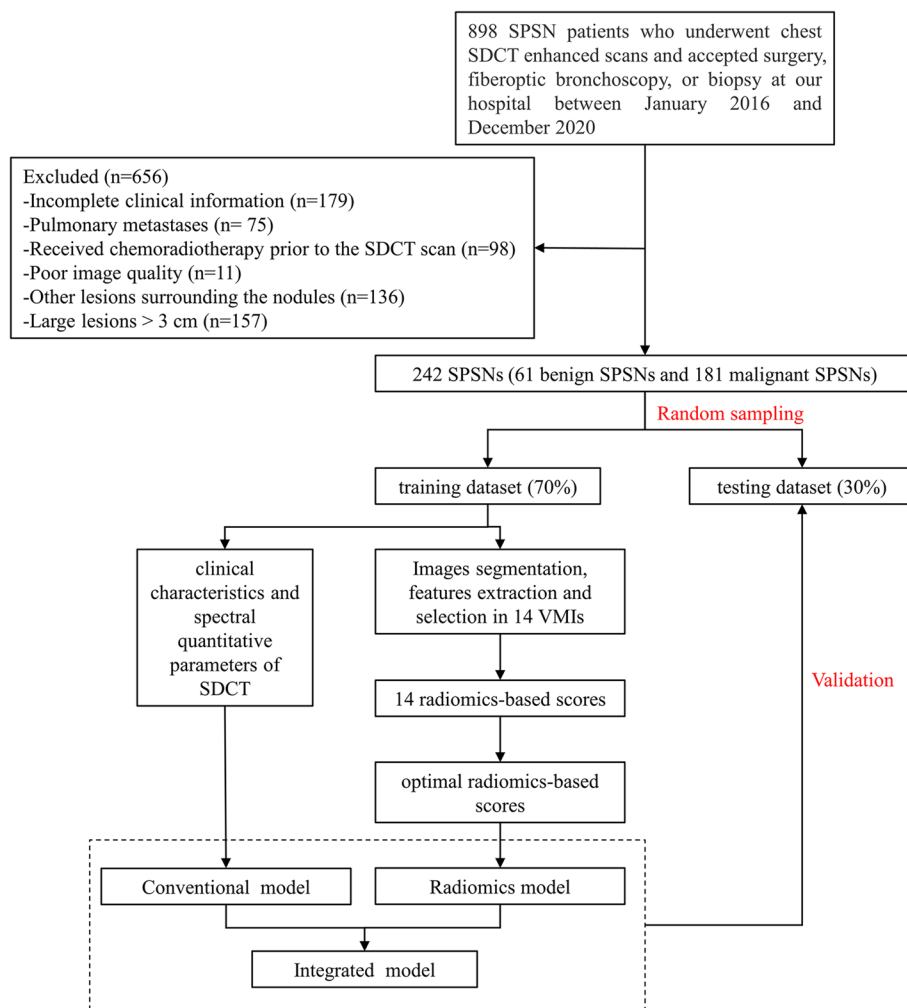
Fig. 1 Overview workflow of this study. SDCT, dual-layer Spectral Detector CT; SPSN, solitary pulmonary solid nodule; VMI, virtual monochromatic images

nodule area on CT images of 40 keV by a radiologist (with 14 years of experience in chest imaging diagnosis) who was blinded to the clinical data and histopathologic results. The copy-and-paste function was used to ensure that the position and size of the ROIs were consistent between different VMIs of SDCT.

Feature extraction, selection, and screen of the optimal sequence of VMI

Radiomics features were extracted from ROIs with the reference of the image biomarker standardization initiative (IBSI) [28] using an artificial intelligence kit (A.K., GE Healthcare), and the data was standardized. In order to ensure stability and robustness of the radiomics features, 30 cases were randomly selected in a blinded manner. The same image segmentation process

and feature extraction were conducted among the 30 cases by another radiologist (with 7 years of experience in chest imaging diagnosis). The intraclass correlation coefficient (ICC) was calculated to test the interobserver reproducibility of the radiomics features. Features with ICC value > 0.75 were considered a good agreement and were used for subsequent analysis [29]. The least absolute shrinkage and selection operator (LASSO) regression was conducted to select the optimal radiomics features with non-zero coefficients via ten-fold cross-validation. Finally, a total of 14 radiomics-based scores were respectively calculated based on optimal radiomics features of 40-65 keV images of AP, VP, and conventional 120kVp by multivariate logistic regression, then the optimal radiomics-based score was screened for subsequent modeling. A radiomics workflow was shown in Fig. 2.
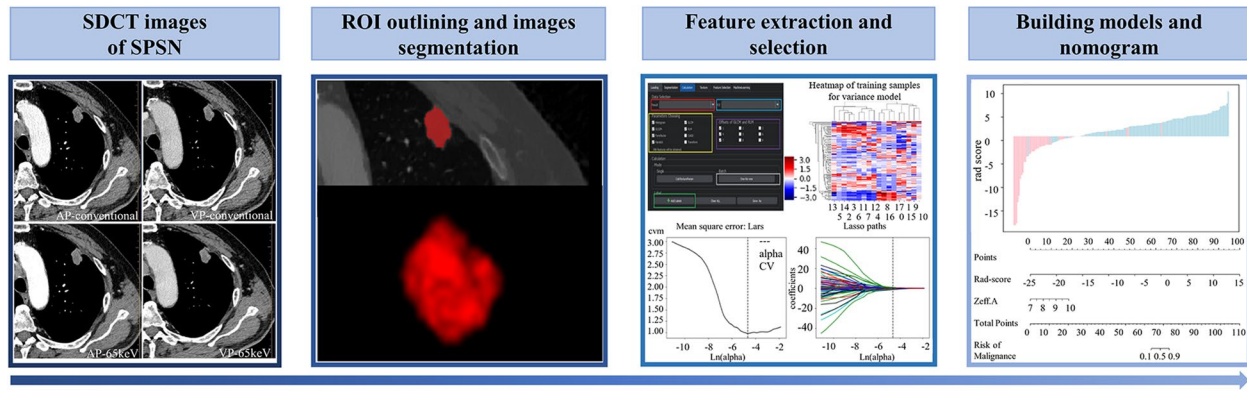
Xu *et al. BMC Cancer*   (2023) 23:91

Page 4 of 10

Fig. 2 A flow chart displaying the process of building radiomics-based model in this study. AP, arterial phase; VP, venous phase; SDCT, dual-layer Spectral Detector CT; SPSN, solitary pulmonary solid nodule; ROI, region of interest

Models building

Significant clinical features and spectral CT quantitative parameters which were selected by univariate logistic regression and Spearman correlations analysis [30], were used to construct the clinical features and spectral CT quantitative parameters-based model. Then we defined it as conventional model. The above-mentioned optimal radiomics-based score was used to establish a radiomics-based model through multivariate logistic regression. Finally, an integrated model incorporating radiomics-based model with conventional model was built by univariate and multivariate logistic regression with stepwise selection method.

Statistical analysis

All statistical analyses were performed with R software (version 3.5.1; http://www.Rproject.org). Quantitative data with normal distribution was presented as mean $S \pm SD$; quantitative data with abnormal distribution was presented as median (25th, 75th percentile). Categorical variables were compared by chi-square test or the Fisher exact test; either Student's t-test or Mann-Whitney U test was used for the continuous variables as appropriate. The level of significance was $p < 0.05$.

Receiver-operating characteristic (ROC) curves were applied to assess the predictive ability of the models in distinguishing benign from malignant SPSNs, and accuracy, sensitivity, specificity, and the area under the curve (AUC) were calculated respectively. The DeLong test was used to compare the AUC between different models or different datasets. Calibration curves were plotted and the Hosmer-Lemeshow test was used to assess the fitness of the models. Decision curves were used to compare the clinical usefulness of models.

Results

Patient characteristics

A total of 242 patients' clinical characteristics and spectral quantitative parameters from SDCT in the training and testing datasets were detailed in Table 1. There were 61 benign SPSNs and 181 malignant SPSNs in this cohort (Supplementary Materials).

Feature selection and optimal VMI sequence screening

A total of 107 radiomics features with interobserver ICC value > 0.75 were extracted from ROIs based on 40-65 keV images of AP, VP, and conventional 120kVp respectively. Then the optimal radiomics features of each sequence remained respectively after LASSO, which were devoted to calculating 14 radiomics-based scores by multivariate logistic regression.

The diagnostic performance of 14 radiomics-based scores was detailed in Supplementary Table A2. Among these, the diagnostic performance based on 65 keV images in both AP and VP was the best in differentiating benign and malignant SPSNs in the training ($AUC_{65keV-AP} = 0.94$, $AUC_{65keV-VP} = 0.92$) and testing datasets ($AUC_{65keV-AP} = 0.92$, $AUC_{65keV-VP} = 0.88$), respectively. The optimal radiomics features of 65 keV radiomics-based scores in AP and VP were displayed respectively in Supplementary Table A3.

Models building

Among the 16 clinical characteristics and spectral quantitative parameters, 14 features were selected by univariate logistic regression, eight features (CEA, Z_{eff-AP}, age, CYFRA21-1, NSE, $CT_{40keV-VP}$, NIC_{AP}, NIC_{VP}) were remained after redundancy with Spearman correlation analysis, which were used to establish conventional model. The radiomics-based scores based

Xu *et al. BMC Cancer*   (2023) 23:91

Page 5 of 10

Table 1 Clinical risk factors of the study population and quantitative parameters from SDCT in the training and testing datasets

Variables	Training Dataset (N = 168)			Testing Dataset (N = 74)			p value
	Benign SPSNs (N = 42)	Malignant SPSNs (N = 126)	p value	Benign SPSNs (N = 19)	Malignant SPSNs (N = 55)	p value	
Male	15(35.71%)	70(55.56%)	0.026*	11(57.89%)	27(49.09%)	0.508	0.914
Age	58.00(49.95, 63.00)	62.00(54.95, 67.00)	0.035*	54.26 ± 11.32	60.87 ± 9.11	0.013*	0.559
Smoking	12(28.57%)	60(47.62%)	0.031*	8(42.11%)	25(45.45%)	0.800	0.802
CEA	2.40(1.40, 3.08)	4.36(2.20, 24.25)	<0.001*	1.99(1.57, 3.06)	4.36(2.53, 25.51)	<0.001*	0.836
CYFRA21-1	2.48(2.10, 2.88)	3.42(2.45, 6.16)	<0.001*	2.20(1.71, 3.62)	3.99(2.31, 5.83)	0.001*	0.975
NSE	14.20(12.31, 15.81)	14.96(13.10, 19.00)	0.018*	13.76(12.48, 14.34)	14.90(12.87, 17.54)	0.089	0.399
IC_{AP}	0.86(0.42, 1.57)	1.23(0.98, 1.66)	0.004*	0.84(0.64, 1.31)	1.36(1.17, 1.90)	<0.001*	0.254
IC_{VP}	1.23 ± 0.89	1.60 ± 0.52	0.014*	0.99 ± 0.68	1.82 ± 0.68	<0.001*	0.302
NIC_{AP}	0.10(0.04, 0.17)	0.13(0.10, 0.16)	0.010*	0.10(0.05, 0.13)	0.15(0.11, 0.19)	<0.001*	0.293
NIC_{VP}	0.27 ± 0.17	0.36 ± 0.10	0.003*	0.20 ± 0.12	0.41 ± 0.15	<0.001*	0.567
$CT_{40keV-AP}$	107.00(68.95, 152.96)	142.30(119.78, 181.00)	0.001*	105.40(78.08, 145.90)	154.10(130.84, 196.44)	<0.001*	0.304
$CT_{40keV-VP}$	137.94 ± 77.43	172.64 ± 44.60	0.008*	114.26 ± 61.03	187.63 ± 49.54	<0.001*	0.551
λ_{HU-AP}	1.45(0.70, 2.39)	2.08(1.64, 2.76)	0.003*	1.43(1.09, 2.19)	2.28(1.96, 3.17)	<0.001*	0.247
λ_{HU-VP}	2.05 ± 1.51	2.62 ± 0.88	0.026*	1.63 ± 1.14	3.03 ± 1.14	<0.001*	0.235
Z_{eff-AP}	7.87(7.60, 8.18)	8.07(7.94, 8.27)	0.002*	7.81 ± 0.33	8.22 ± 0.36	<0.001*	0.164
Z_{eff-VP}	7.92(7.58, 8.33)	8.18(8.06, 8.38)	0.001*	7.81(7.68, 8.20)	8.32(8.14, 8.48)	<0.001*	0.239

SDCT Dual-layer spectral detector CT, *CEA* Carcinoembryonic antigen, *CYFRA21-1* Cytokeratin 19 fragment 21-1, *NSE* Neuron-specific enolase, *IC* Iodine concentration, *NIC* Normalized iodine concentration, CT_{40keV} CT values of 40 keV monochromatic images, λ_{HU} Dual-energy curve slope value, Z_{eff} Effective atomic number, *AP* Arterial phase, *VP* Venous phase

p values reflected the differences between benign SPSNs and malignant SPSNs, p values reflected the differences between the training and testing datasets, and p values and p values were computed by using Student's t-test or Mann-Whitney U test for continuous variables and chi-square test or the Fisher exact test for categorical data

* in the upper right indicates $p < 0.05$

on 65 keV images of AP and VP were combined to build the radiomics model by multivariate logistic regression. Combined conventional model with radiomics model, eight features (CEA, age, CYFRA21-1, $CT_{40keV-VP}$, score of radiomics $model_{65keV}$, Z_{eff-AP}, NIC_{VP}, NSE) were selected by univariate logistic regression, two features (score of radiomics $model_{65keV}$, Z_{eff-AP}) were remained after multivariate logistic regression, which were committed to developing an integrated model. We presented it as a nomogram in Fig. 3. The calculation
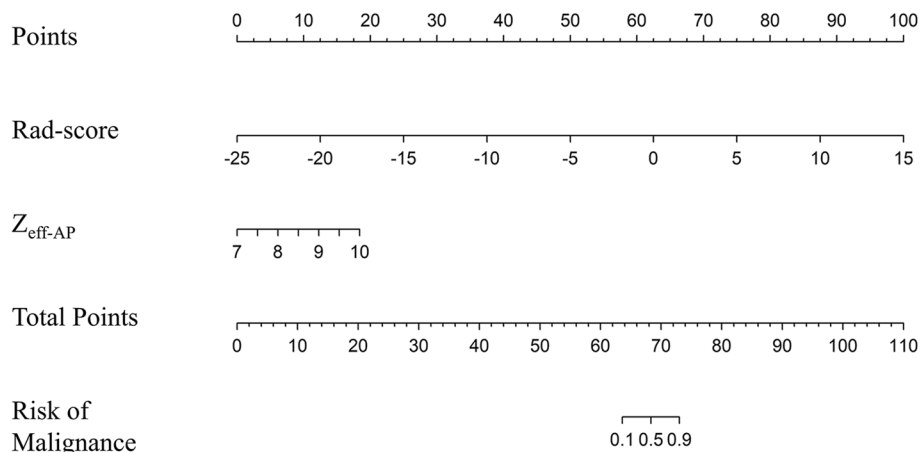

Fig. 3 Developed integrated model nomogram. The integrated model nomogram was built in training dataset with Z_{eff-AP} and a Rad-score of the selected radiomics features incorporated. Z_{eff-AP}, effective atomic number in arterial phase; Rad-score, the score of spectral CT-based radiomics model combining radiomics scores based on 65 keV images of arterial phase and venous phase

Xu *et al. BMC Cancer*   (2023) 23:91

Page 6 of 10

formulas for three models were shown in Supplementary Materials.

Performance evaluation

The diagnostic performance of three models in differentiating between benign and malignant SPSNs was shown in Table 2. ROC curves demonstrated that radiomics model ($AUC_{training} = 0.96$, $AUC_{testing} = 0.96$) outperformed conventional model ($AUC_{training} = 0.88$, $AUC_{testing} = 0.86$) (DeLong test, $P_{training} < 0.01$, $P_{testing} < 0.05$) in differentiating benign and malignant SPSNs in the training and testing datasets, while the integrated model was further slightly improved ($AUC_{training} = 0.97$, $AUC_{testing} = 0.97$) (Fig. 4 a, b), but there was no significant difference (DeLong test, $P_{training} = 0.51$, $P_{testing} = 0.72$) of discriminating ability between radiomics model and integrated model. DeLong test revealed that there was no statistical difference in the diagnostic efficacy of three models between the training and testing datasets with *p* values of 0.65, 0.84, and 0.89, respectively. Through the Hosmer-Lemeshow test, calibration curves indicated that there was a good fitness between prediction and observation for the discrimination probability of SPSNs (Fig. 4 c, d). Decision curves suggested that radiomics model and integrated model had higher clinical net benefit than conventional model (Fig. 4 e, f).

Discussion

The results of our study showed that radiomics scores based on 65 keV images of AP and VP from SDCT had the optimal performance within the range of 40-65 keV in the discrimination of benign and malignant SPSNs. Furthermore, we developed and validated a radiomics-based model based on optimal radiomics-based scores derived from 65 keV images of AP and VP, which had better diagnostic performance than conventional model, and the integrated model combining radiomics model and $Z_{eff\text{-}AP}$ that was retained by multiple features screenings

of clinical features and spectral quantitative parameters could further improve the discriminating ability slightly.

To the best of our knowledge, this is the first time to compare the performance of radiomics scores based on different keV VMIs of SDCT to distinguish benign and malignant SPSNs. Currently, in view of clinical need for image quality and resolution, we could obtain 161 monochromatic images between 40-200 keV from spectral CT. Low keV images could improve the density resolution of images and help optimize the display of low-contrast structures, as one of the important clinical applications of VMIs. Given that the reconstruction of 70 keV VMIs is roughly equivalent to a standard spectral CT acquisition performed at 120 kVp [31, 32], our study selected 40-65 keV VMIs to perform radiomics analysis. According to our results, radiomics-based scores varied with different energy levels, the higher energy level, the better diagnostic performance. We did not observe conceivable benefits of greater iodine-related attenuation at lower energy levels when noise tends to be constant low [17, 18] in our radiomics study. It was inconsistent with the assessment by Wen et al. [20] who confirmed that VMIs at 40 keV from SDCT may be an effective way to characterize solitary pulmonary nodules. It may be that overhigh contrast within the lesions covers subtle changes of features, which leads to the error of pixel information extraction in our radiomics study.

An additional important observation was that radiomics model was significantly better than conventional model, indicating the advantages of radiomics features obtained from SDCT in the identification of SPSNs. The top two radiomics features with the greatest relative weights obtained from training dataset in radiomics model were GLCM-Cluster-Prominence of AP and GLRLM-Short-Run-High-Gray-Level-Emphasis of VP. The former revealed larger asymmetry [33] and the latter revealed higher and more heterogeneous iodine uptake, and greater images roughness [34, 35], which indicated more complex histological architecture with malignant

Table 2 Comparison of AUCs between the radiomics model, conventional model, and integrated model

Model	Cut-off	Training dataset				Testing dataset			
		AUC (95%CI)	SEN	SPE	ACC	AUC (95%CI)	SEN	SPE	ACC
Radiomics model	0.91	0.96 (0.925–0.996)	0.94	0.91	0.92	0.96 (0.914–0.996)	0.87	0.90	0.87
Conventional model	0.60	0.88 (0.823–0.941)	0.86	0.81	0.84	0.86 (0.767–0.948)	0.82	0.70	0.76
Integrated model	1.01	0.97 (0.940–0.997)	0.91	0.93	0.91	0.97 (0.928–1.000)	0.91	0.95	0.92

AUC Area under ROC curve, *95% CI* 95% confidence interval, *SEN* Sensitivity, *SPE* Specificity, *ACC* Accuracy, *Radiomics model* The model combining optimal radiomics scores based on 65 keV images of AP and VP, *Conventional model* The model based on significant clinical characteristics and spectral quantitative parameters, *Integrated model* The model combining radiomics model and $Z_{eff\text{-}AP}$
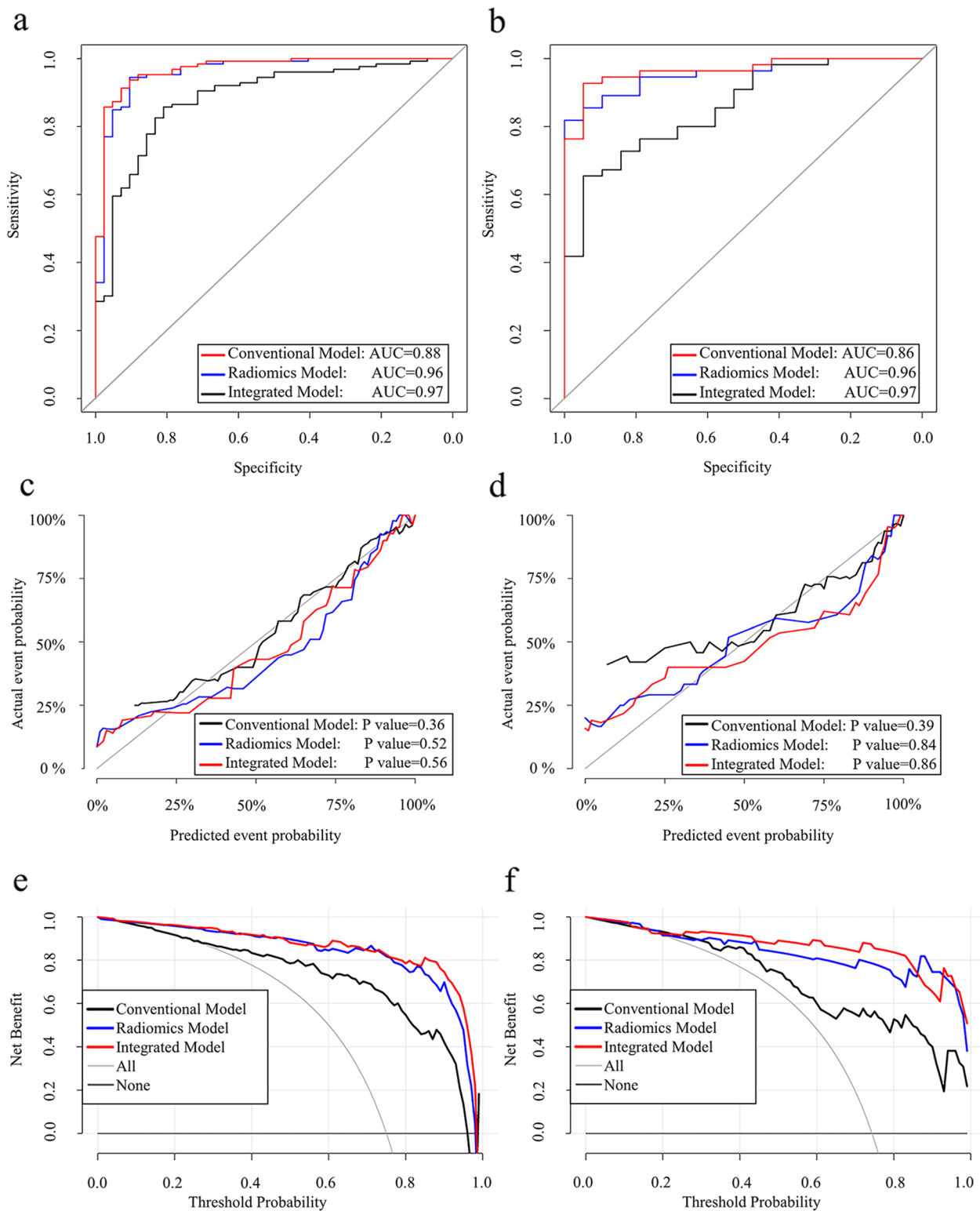
Fig. 4 The performance of three models in distinguishing benign from malignant SPSNs. ROC curves for radiomics model, conventional model, and integrated model in training (**a**) and testing datasets (**b**). Calibration curves for radiomics model, conventional model, and integrated model in training (**c**) and testing datasets (**d**). The calibration curves described a good fitness of three models between prediction and observation of the benign and malignant SPSNs. The gray line represented the perfect prediction. A closer fitness to the gray line represented a well-calibrated model. Decision curves for radiomics model, conventional model, and integrated model in training (**e**) and testing datasets (**f**). Integrated model and radiomics model had higher net benefit than conventional model. SPSN, solitary pulmonary solid nodule

Xu *et al. BMC Cancer*   (2023) 23:91

Page 8 of 10

SPSNs. In our study, radiomics model also displayed higher diagnostic efficacy than previous conventional CT radiomics-based models regarding the qualitative diagnosis of pulmonary nodule [4, 5, 7–9], whose comparison was detailed in Supplementary Table A4. Among them, the deep learning model [4, 7], the machine learning model built with intranodular and perinodular features combined [4], and the contrast-enhanced CT radiomics-based model [5] all failed to increase more valid discriminating capability of the nature of SPSNs then spectral CT radiomics-based model. The above results may be attributed to two major points: Firstly, spatial and temporal alignment completely is ideal for data collection. Secondly, the combination of radiomics features in AP and VP can more comprehensively reflect the mixed distribution state of different nodules owing to vascular permeability or inflammatory components. It may be possible to contribute to selecting radiomics features, and increase the efficiency of identification in benign and malignant SPSNs. However, Zhuo et al. [6] generated a more predictive radiomics model in differentiating nature of SPSNs including adenocarcinoma and tuberculosis, which may be attributed to the fact that our study involved more clinically relevant samples with multiple types of SPSNs, not limited to the distinction between tuberculosis and adenocarcinoma. Besides, the patient population ratio of adenocarcinoma was lower than tuberculosis in their study, which went against the usual constituent ratio in clinical, in which pulmonary nodules with fewer signs of malignant are generally less likely to undergo a biopsy or surgery.

Moreover, we developed an integrated model based on radiomics model and Z_{eff-AP}, which were combined together for the first time, the accuracy was improved from 87% to 92%, and the sensitivity and specificity were improved from 87% and 90% to 91% and 95%, respectively. Z_{eff} is a quantitative index derived from atomic number, representing the composite atom for a mixture or compound of various materials, and it can be calculated from dual-energy spectral computed tomography data [36] and applied to identify substance composition. The role of Z_{eff} in differentiating benign and malignant lung tumors was firstly reported by Gonzalez-perez, V. et al. [36]. Subsequently, the values of Z_{eff} in detecting tumor progression [37], evaluating histological types of lung cancer [21, 38], as well as taking part in gene expression [39] were discovered. The above results also remained that traditional spectral quantitative parameters may still reveal utility in differentiating benign and malignant SPSNs. Consequently, multi-dimensional consideration and analysis are required.

This study still has some limitations. Firstly, the sample size of our study was relatively small along with a large proportion of malignant SPSNs (75%) in our cohort, which may result in selection bias and exaggerate the diagnostic efficacy of predictive models to some extent, the efficacy of our models needs to be further validated in a large population. Secondly, the clinical application of our predictive models to general populations was limited to a single-center study, thus there is still a requirement for further verifying our models in a multi-center and independent validation cohort. Thirdly, no subgroup analysis of SPSNs was conducted in this study, further research based on spectral CT radiomics in the differentiation of tumor subtyping will be carried out. Finally, retrospective data collection may also lead to sample bias, and further prospective studies are still required.

Conclusion

Among the 40-65 keV radiomics scores based on SDCT, 65 keV radiomics-based score had the optimal performance in distinguishing benign from malignant pulmonary nodules. The developed integrated model based on radiomics model and Z_{eff-AP} was significantly superior to conventional model in the discrimination of SPSNs. This method had the potential to reveal the heterogeneity of nodules and provided accurate information for the nature of SPSNs, which would serve to provide individual medical services for patients with SPSNs efficiently and scientifically.

Supplementary Information

Additional file 1: Table A1. Pathologic results of the study population. **Table A2.** Comparison of diagnostic efficacy of radiomics scores based on 40-65keV images of arterial and venous phases and conventional 120kVp images from SDCT in the training and testing datasets. **Table A3.** Optimal radiomics features based on 65keV images of arterial and venous phases of SDCT. **Table A4.** General characteristics and main results of included studies in the discussion. **Figure A1.** Feature selection of LASSO regression in 65keV images of arterial phase. **Figure A2.** Feature selection of LASSO regression in 65keV images of venous phase. **Figure A3.** Heatmaps of the significant radiomics features derived from 65keV images. **Figure A4.** Bar chart for the radiomics model in the training (4a) and testing datasets (4b). **Figure A5.** Bar chart for the conventional model in the training (5a) and testing datasets (5b). **Figure A6.** Bar chart for the integrated model in the training (6a) and testing datasets (6b).

Xu *et al. BMC Cancer*   (2023) 23:91

Page 9 of 10

Availability of data and materials
Our study's source code was uploaded at https://github.com/lszxuhang/zhuna-final.git. And the datasets generated during this study were available in the [Data of 242 patients] repository, [https://doi.org/10.6084/m9.figshare.21800861].

Declarations

Ethics approval and consent to participate
This retrospective study was approved by the Medical Ethics Committee of Shengjing Hospital of China Medical University (No. 2021PS066K) and in conformity to the Declaration of Helsinki. The need for informed consent of participants in this study was waived by ethics committee of Shengjing Hospital of China Medical University (No. 2021PS066K).

Consent for publication
Not applicable.

Competing interests
The authors declare that they have no competing interests.

References
1. Khawaja A, Bartholmai BJ, Rajagopalan S, Karwoski RA, Varghese C, Maldonado F, Peikert T. Do we need to see to believe?-radiomics for lung nodule classification and lung cancer risk stratification. J Thorac Dis. 2020;12(6):3303–16. https://doi.org/10.21037/jtd.2020.03.105.
2. Dennie C, Thornhill R, Sethi-Virmani V, Souza CA, Bayanati H, Gupta A, Maziak D. Role of quantitative computed tomography texture analysis in the differentiation of primary lung cancer and granulomatous nodules. Quant Imaging Med Surg. 2016;6(1):6–15. https://doi.org/10.3978/j.issn.2223-4292.2016.02.01.
3. Alilou M, Beig N, Orooji M, Rajiah P, Velcheti V, Rakshit S, Reddy N, Yang M, Jacono F, Gilkeson RC, Linden P, Madabhushi A. An integrated segmentation and shape-based classification scheme for distinguishing adenocarcinomas from granulomas on lung CT. Med Phys. 2017;44(7):3556–69. https://doi.org/10.1002/mp.12208.
4. Beig N, Khorrami M, Alilou M, Prasanna P, Braman N, Orooji M, Rakshit S, Bera K, Rajiah P, Ginsberg J, Donatelli C, Thawani R, Yang M, Jacono F, Tiwari P, Velcheti V, Gilkeson R, Linden P, Madabhushi A. Perinodular and Intranodular Radiomic Features on Lung CT Images Distinguish Adenocarcinomas from Granulomas. Radiology. 2019;290(3):783–92. https://doi.org/10.1148/radiol.2018180910.
5. Yang X, He J, Wang J, Li W, Liu C, Gao D, Guan Y. CT-based radiomics signature for differentiating solitary granulomatous nodules from solid lung adenocarcinoma. Lung Cancer. 2018;125:109–14. https://doi.org/10.1016/j.lungcan.2018.09.013.
6. Zhuo Y, Zhan Y, Zhang Z, Shan F, Shen J, Wang D, Yu M. Clinical and CT Radiomics Nomogram for Preoperative Differentiation of Pulmonary Adenocarcinoma From Tuberculoma in Solitary Solid Nodule. Front Oncol. 2021;11:701598. https://doi.org/10.3389/fonc.2021.701598.
7. Feng B, Chen X, Chen Y, Lu S, Liu K, Li K, Liu Z, Hao Y, Li Z, Zhu Z, Yao N, Liang G, Zhang J, Long W, Liu X. Solitary solid pulmonary nodules: a CT-based deep learning nomogram helps differentiate tuberculosis granulomas from lung adenocarcinomas. Eur Radiol. 2020;30(12):6497–507. https://doi.org/10.1007/s00330-020-07024-z.
8. Feng B, Chen X, Chen Y, Liu K, Li K, Liu X, Yao N, Li Z, Li R, Zhang C, Ji J, Long W. Radiomics nomogram for preoperative differentiation of lung tuberculoma from adenocarcinoma in solitary pulmonary solid nodule.

Eur J Radiol. 2020;128:109022. https://doi.org/10.1016/j.ejrad.2020.109022.
9. Liu A, Wang Z, Yang Y, Wang J, Dai X, Wang L, Lu Y, Xue F. Preoperative diagnosis of malignant pulmonary nodules in lung cancer screening with a radiomics nomogram. Cancer Commun (Lond). 2020;40(1):16–24. https://doi.org/10.1002/cac2.12002.
10. Forghani R. An update on advanced dual-energy CT for head and neck cancer imaging. Expert Rev Anticancer Ther. 2019;19(7):633–44. https://doi.org/10.1080/14737140.2019.1626234.
11. Forghani R, Chatterjee A, Reinhold C, Perez-Lara A, Romero-Sanchez G, Ueno Y, Bayat M, Alexander JWM, Kadi L, Chankowsky J, Seuntjens J, Forghani B. Head and neck squamous cell carcinoma: prediction of cervical lymph node metastasis by dual-energy CT texture analysis with machine learning. Eur Radiol. 2019;29(11):6172–81. https://doi.org/10.1007/s00330-019-06159-y.
12. Al Ajmi E, Forghani B, Reinhold C, Bayat M, Forghani R. Spectral multi-energy CT texture analysis with machine learning for tissue classification: an investigation using classification of benign parotid tumours as a testing paradigm. Eur Radiol. 2018;28(6):2604–11. https://doi.org/10.1007/s00330-017-5214-0.
13. Hsu CC, Jeavon C, Fomin I, Du L, Buchan C, Watkins TW, Nae Y, Parry NM, Aviv RI. Dual-Layer Spectral CT Imaging of Upper Aerodigestive Tract Cancer: Analysis of Spectral Imaging Parameters and Impact on Tumor Staging. AJNR Am J Neuroradiol. 2021;42(9):1683–9. https://doi.org/10.3174/ajnr.A7239.
14. Y. Yu, Y. Fu, X. Chen, Y. Zhang, F. Zhang, X. Li, X. Zhao, J. Cheng, H. Wu, Dual-layer spectral detector CT: predicting the invasiveness of pure ground-glass adenocarcinoma, Clin Radiol (2022). https://doi.org/10.1016/j.crad.2022.02.006.
15. Moon JI, Choi BH, Baek HJ, Ryu KH, Park SE, Ha JY, Jung EJ, Lee HS, An HJ. Comprehensive analyses with radiological and biological markers of breast cancer on contrast-enhanced chest CT: a single center experience using dual-layer spectral detector CT. Eur Radiol. 2020;30(5):2782–90. https://doi.org/10.1007/s00330-019-06615-9.
16. Lennartz S, Zopfs D, Abdullayev N, Bratke G, Le Blanc M, Slebocki K, Wagner A, Wybranski C, Wahba R, Maintz D, Grosse Hokamp N, Persigehl T. Iodine overlays to improve differentiation between peritoneal carcinomatosis and benign peritoneal lesions. Eur Radiol. 2020;30(7):3968–76. https://doi.org/10.1007/s00330-020-06729-5.
17. Doerner J, Hauger M, Hickethier T, Byrtus J, Wybranski C, Grosse Hokamp N, Maintz D, Haneder S. Image quality evaluation of dual-layer spectral detector CT of the chest and comparison with conventional CT imaging. Eur J Radiol. 2017;93:52–8. https://doi.org/10.1016/j.ejrad.2017.05.016.
18. Sellerer T, Noel PB, Patino M, Parakh A, Ehn S, Zeiter S, Holz JA, Hammel J, Fingerle AA, Pfeiffer F, Maintz D, Rummeny EJ, Muenzel D, Sahani DV. Dual-energy CT: a phantom comparison of different platforms for abdominal imaging. Eur Radiol. 2018;28(7):2745–55. https://doi.org/10.1007/s00330-017-5238-5.
19 Rassouli N, Etesami M, Dhanantwari A, Rajiah P. Detector-based spectral CT with a novel dual-layer technology: principles and applications. Insights Imaging. 2017;8(6):589–98. https://doi.org/10.1007/s13244-017-0571-4.
20 Wen Q, Yue Y, Shang J, Lu X, Gao L, Hou Y. The application of dual-layer spectral detector computed tomography in solitary pulmonary nodule identification. Quant Imaging Med Surg. 2021;11(2):521–32. https://doi.org/10.21037/qims-20-2.
21 Jia Y, Xiao X, Sun Q, Jiang H. CT spectral parameters and serum tumour markers to differentiate histological types of cancer histology. Clin Radiol. 2018;73(12):1033–40. https://doi.org/10.1016/j.crad.2018.07.104.
22. Wu L, Cao G, Zhao L, Tang K, Lin J, Miao S, Lin T, Sun J, Zheng X. Spectral CT Analysis of Solitary Pulmonary Nodules for Differentiating Malignancy from Benignancy: The Value of Iodine Concentration Spatial Distribution Difference. Biomed Res Int. 2018;2018:4830659. https://doi.org/10.1155/2018/4830659.
23. Zegadlo A, Zabicka M, Kania-Pudlo M, Maliborski A, Rozyk A, Sosnicki W. Assessment of Solitary Pulmonary Nodules Based on Virtual Monochrome Images and Iodine-Dependent Images Using a Single-Source Dual-Energy CT with Fast kVp Switching. J Clin Med. 2020;9(8):2514. https://doi.org/10.3390/jcm9082514.
24 Zhang Y, Cheng J, Hua X, Yu M, Xu C, Zhang F, Xu J, Wu H. Can Spectral CT Imaging Improve the Differentiation between Malignant and Benign

Xu *et al. BMC Cancer*   (2023) 23:91

Page 10 of 10

Solitary Pulmonary Nodules? PLoS One. 2016;11(2):e0147537. https://doi.org/10.1371/journal.pone.0147537.

25. Apfaltrer P, Meyer M, Meier C, Henzler T, Barraza JM Jr, Dinter DJ, Hohenberger P, Schoepf UJ, Schoenberg SO, Fink C. Contrast-enhanced dual-energy CT of gastrointestinal stromal tumors: is iodine-related attenuation a potential indicator of tumor response? Invest Radiol. 2012;47(1):65–70. https://doi.org/10.1097/RLI.0b013e31823003d2.

26. Wu F, Zhou H, Li F, Wang JT, Ai T. Spectral CT Imaging of Lung Cancer: Quantitative Analysis of Spectral Parameters and Their Correlation with Tumor Characteristics. Acad Radiol. 2018;25(11):1398–404. https://doi.org/10.1016/j.acra.2018.04.017.

27. Hou WS, Wu HW, Yin Y, Cheng JJ, Zhang Q, Xu JR. Differentiation of lung cancers from inflammatory masses with dual-energy spectral CT imaging. Acad Radiol. 2015;22(3):337–44. https://doi.org/10.1016/j.acra.2014.10.004.

28. A. Zwanenburg, M. Vallieres, M.A. Abdalah, H. Aerts, V. Andrearczyk, A. Apte, S. Ashrafinia, S. Bakas, R.J. Beukinga, R. Boellaard, M. Bogowicz, L. Boldrini, I. Buvat, G.J.R. Cook, C. Davatzikos, A. Depeursinge, M.C. Desseroit, N. Dinapoli, C.V. Dinh, S. Echegaray, I. El Naqa, A.Y. Fedorov, R. Gatta, R.J. Gillies, V. Goh, M. Gotz, M. Guckenberger, S.M. Ha, M. Hatt, F. Isensee, P. Lambin, S. Leger, R.T.H. Leijenaar, J. Lenkowicz, F. Lippert, A. Losnegard, K.H. Maier-Hein, O. Morin, H. Muller, S. Napel, C. Nioche, F. Orlhac, S. Pati, E.A.G. Pfaehler, A. Rahmim, A.U.K. Rao, J. Scherer, M.M. Siddique, N.M. Sijtsema, J. Socarras Fernandez, E. Spezi, R. Steenbakkers, S. Tanadini-Lang, D. Thorwarth, E.G.C. Troost, T. Upadhaya, V. Valentini, L.V. van Dijk, J. van Griethuysen, F.H.P. van Velden, P. Whybra, C. Richter, S. Lock, The Image Biomarker Standardization Initiative: Standardized Quantitative Radiomics for High-Throughput Image-based Phenotyping, Radiology 295(2) (2020) 328–338.https://doi.org/10.1148/radiol.2020191145.

29. Koo TK, Li MY. A Guideline of Selecting and Reporting Intraclass Correlation Coefficients for Reliability Research. J Chiropr Med. 2016;15(2):155–63. https://doi.org/10.1016/j.jcm.2016.02.012.

30. Wu G, Woodruff HC, Shen J, Refaee T, Sanduleanu S, Ibrahim A, Leijenaar RTH, Wang R, Xiong J, Bian J, Wu J, Lambin P. Diagnosis of Invasive Lung Adenocarcinoma Based on Chest CT Radiomic Features of Part-Solid Pulmonary Nodules: A Multicenter Study. Radiology. 2020;297(2):451–8. https://doi.org/10.1148/radiol.2020192431.

31. Perez-Lara A, Forghani R. Spectral Computed Tomography: Technique and Applications for Head and Neck Cancer. Magn Reson Imaging Clin N Am. 2018;26(1):1–17. https://doi.org/10.1016/j.mric.2017.08.001.

32. Forghani R. Advanced dual-energy CT for head and neck cancer imaging. Expert Rev Anticancer Ther. 2015;15(12):1489–501. https://doi.org/10.1586/14737140.2015.1108193.

33. Huang SY, Franc BL, Harnish RJ, Liu G, Mitra D, Copeland TP, Arasu VA, Kornak J, Jones EF, Behr SC, Hylton NM, Price ER, Esserman L, Seo Y. Exploration of PET and MRI radiomic features for decoding breast cancer phenotypes and prognosis. NPJ Breast Cancer. 2018;4:24. https://doi.org/10.1038/s41523-018-0078-2.

34. Saleem BR, Beukinga RJ, Boellaard R, Glaudemans AW, Reijnen MM, Zeebregts CJ, Slart RH. Textural features of (18)F-fluorodeoxyglucose positron emission tomography scanning in diagnosing aortic prosthetic graft infection. Eur J Nucl Med Mol Imaging. 2017;44(5):886–94. https://doi.org/10.1007/s00259-016-3599-7.

35. Zheng X, Li C, Zhang L, Cao F, Fang X, Qian L, Dong J. Combining Intravoxel Incoherent Motion Diffusion Weighted Imaging and Texture Analysis for a Nomogram to Predict Early Treatment Response to Concurrent Chemoradiotherapy in Cervical Cancer Patients. J Oncol. 2021;2021:9345353. https://doi.org/10.1155/2021/9345353.

36. Gonzalez-Perez V, Arana E, Barrios M, Bartres A, Cruz J, Montero R, Gonzalez M, Deltoro C, Martinez-Perez E, De Aguiar-Quevedo K, Arraras M. Differentiation of benign and malignant lung lesions: Dual-Energy Computed Tomography findings. Eur J Radiol. 2016;85(10):1765–72. https://doi.org/10.1016/j.ejrad.2016.07.019.

37. Tomita K, Hiraki T, Gobara H, Fujiwara H, Iguchi T, Matsui Y, Kanazawa S. Evaluation of Lung Radiofrequency Ablation With Dual-Energy Computed Tomography: Analysis of Tumor Composition and Lung Perfusion. J Comput Assist Tomogr. 2016;40(5):752–6. https://doi.org/10.1097/RCT.0000000000000422.

38. Deniffel D, Sauter A, Fingerle A, Rummeny EJ, Makowski MR, Pfeiffer D. Improved differentiation between primary lung cancer and pulmonary metastasis by combining dual-energy CT-derived biomarkers with

conventional CT attenuation. Eur Radiol. 2021;31(2):1002–10. https://doi.org/10.1007/s00330-020-07195-9.

39. Zhang G, Cao Y, Zhang J, Zhao Z, Zhang W, Zhou J. Epidermal growth factor receptor mutations in lung adenocarcinoma: associations between dual-energy spectral CT measurements and histologic results. J Cancer Res Clin Oncol. 2021;147(4):1169–78. https://doi.org/10.1007/s00432-020-03402-8.

Publisher's Note